Journal of Materials Chemistry C

Refractory metal-based photonic narrowband emitter for thermophotovoltaic energy conversion

Journal:	*Journal of Materials Chemistry C*
Manuscript ID	TC-ART-11-2022-004644.R1
Article Type:	Paper
Date Submitted by the Author:	04-Jan-2023
Complete List of Authors:	Chen, Fangqi; Northeastern University Liu, Xiaojie; Northeastern University Liu, Yang; Northeastern University, Mechanical Engineering Tian, Yanpei; Northeastern University, ME Zheng, Yi; Northeastern University, Mechanical Engineering

Journal Name

ARTICLE TYPE

Cite this: DOI: 00.0000/xxxxxxxxxx

Refractory metal-based photonic narrowband emitter for thermophotovoltaic energy conversion†

Fangqi Chen,[a] Xiaojie Liu,[a] Yang Liu,[a] Yanpei Tian,[a] and Yi Zheng*[a,b]

Received Date
Accepted Date

DOI: 00.0000/xxxxxxxxxx

Thermophotovoltaics is a promising technology for heat recovery and has garnered tremendous attention in the past decades. In the thermophotovoltaics system, a selective emitter is required to convert the incoming light in order to emit appropriate photons matched with the bandgap of the PV cell, both avoiding low-energy useless photons and thermalization loss caused by high-energy photons. This work aims to design a metal-based photonic narrowband emitter, and it is composed of tungsten, a refractory material which can withstand the high working temperature of the thermophotovoltaics system. Besides, the advantage of the all-metal emitter is that there is no concern of thermal expansion mismatch. Hexagon and square patterned arrays are numerically analyzed and a parametric study is conducted for different feature sizes, gaps, and pattern heights, leading to emission peak shift and bandwidth change. Besides, the photonic metal-based emitter is fabricated utilizing photolithography method, optically characterized and compared with the calculated emissivity spectra. This work sheds light on the research of high-temperature thermal management, energy harvesting and power generation.

1 Introduction

Energy conversion by single-junction solar cells is restricted by the Shockley–Queisser limit[1]. There are two factors causing this limitation: photons with energy below the bandgap of solar cells cannot generate electron–hole pairs; photons with energy higher than the bandgap can at most generate one electron–hole pair in most cases, which results in the thermalization loss and lower conversion efficiency[2]. In recent years, two main developments in the research field of photovoltaics have been witnessed: the cost reduction in crystalline Si photovoltaics[3] and the rise of a new class of photovoltaic absorber materials, the metal-halide perovskites[4–8]. On the other hand, by tailoring the incoming solar radiation spectrum into desirable narrowband thermal emission, thermophotovoltaic (TPV) is a promising method to harvest the solar energy and enhance the conversion efficiency. A typical TPV system is composed of three components: a heat source, a selective thermal emitter (or a broadband emitter with a filter) and a TPV cell[9]. The heat sources for the TPV system include the combustion of fuels, concentrated solar or nuclear energy, and industrial waste heat[10]. When utilizing solar energy, the system is also called solar thermophotovoltaic (STPV). Compared with a solar photovoltaic (PV) system, the flexibility of converting various heat energy sources enables the TPV system to work for a longer operation time. Besides, the TPV system possesses merits of mechanical stability, large power output and noiselessness, rendering it promising for abundant applications, including STPV systems[11,12], waste heat recovery[13,14], thermal energy storage system[15,16], space applications[17,18], and combustion-driven TPV generators[19,20].

In order to optimize the conversion efficiency of the TPV system, emitters with a tailored spectrum are often utilized to block low-energy photons that may result in an overheating effect. Emitters are categorized into two types: broadband emitters and selective emitters. A broadband emitter has a high emissivity over a large wavelength range, and its radiative spectral heat flux is similar to that of a black body, referring to it as a gray body[21]. The broadband emitters radiate more photons to the cell, and a higher output power is also obtained. However, device heating from thermalization, impaired device performance and reduced conversion efficiency would possibly occur[22]. Therefore, a tailored selective emitter is preferred. A selective thermal emitter transmits electromagnetic energy by tuning heat from sources into an emission spectrum according to the bandgap of the cell[23]. The emission spectrum should match the bandgap of the TPV cell, and the low-energy photons need to be eliminated as far as possible to avoid thermal leakage, which has a negative effect on the conversion efficiency of the system[9]. The emissivity for an ideal TPV narrowband emitter is unity in the wavelength range corresponding to the TPV cell bandgap, while it is zero in the remaining range. On contrary to the broadband emitter, the selective emitter exhibits higher efficiency but relatively lower output. Therefore,

[a] Department of Mechanical and Industrial Engineering, Northeastern University, Boston, MA 02115, USA.
[b] Department of Electrical and Computer Engineering, Northeastern University, Boston, MA 02115, USA.

there exists a compromise between power and efficiency to maximize the benefit of a practical application.

Metamaterials or metasurfaces consisting of patterned subwavelength structures have been widely employed for thermal emission control[24–27]. There are quite a few review papers about selective emitters[28–30]. Sakakibara et al. reviewed the state-of-the-art practical emitters and presented five metrics for a comprehensive evaluation[31], which include optical performance, scalability of fabrication, high-temperature stability for a long-term usage, expense and convenience of integration within the whole system. For the most practical emitter implementation, emitters used in prototype system demonstrations are categorized based on the structure, including bulk emitters[32,33], naturally selective emitters made of rare earth metals[34], 1D photonic crystal[35,36], 2D photonic crystal [37,38], and multilayer stack composed of subwavelength metal and dielectric layers[39,40]. Tian et al. reviewed tunable radiative wavelength selectivity of nanometamaterials in both near-field and far-field radiative heat transfer[41]. Diverse structures of metamaterials were demonstrated, including nanoparticle-embedded structures, grating and multilayered structures. In this paper, we first numerically design a tungsten patterned array narrowband emitter. Tungsten is a commonly used refractory metal as the emitter material, which is more promising to achieve high-temperature stability. A parametric study is conducted for two shape types of the patterned array, hexagon and square. Then, the emitter is fabricated utilizing photolithography method. A comparison of the emissivity spectra is shown between the calculation and experiment.

2 Results and discussion

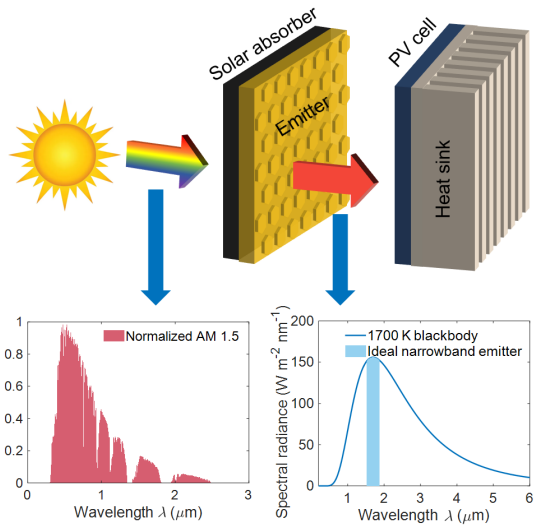

Fig. 1 Schematic of the STPV system, which is composed of three components: a heat source (concentrated sunlight), an intermediate absorber-emitter module and a TPV cell. The emitter works at a high temperature and converts broadband solar radiation into narrowband thermal emission. An ideal narrowband emitter can take full advantage of the most appropriate photons matched with the bandgap of the PV cell.

Figure 1 shows the schematic of the STPV system. The incident solar spectrum covers a wavelength range from ultraviolet to near-infrared (AM 1.5). An intermediate absorber-emitter module is utilized to convert broadband solar radiation into narrowband thermal emission. Selective absorption/emission for the absorber–emitter module can be obtained with photonic crystals[42,43], multilayer cavities[44,45], nanowire[46,47], film-coupled metamaterials[48–50] and nanoparticle-based structures[51,52]. Selective absorber with low emissivity in the infrared range helps to restrain the thermal re-emission, suppressing energy dissipation. Carbon-based materials are also popular choices for solar absorbers, such as carbon nanotubes. The absorber is out of interest in this paper. The solar radiation spectrum is tailored into desirable narrowband thermal emission by photonic structure-based selective emitter. The emissivity for an ideal TPV narrowband emitter is unity in the wavelength range corresponding to the TPV cell bandgap, while it is zero in the remaining range. Based on Wien's displacement law, the peak wavelength of thermal radiation for a 1700 K blackbody is 1.7 μm, which matches the bandgap of the GaSb cell (0.72 eV). The ideal narrowband emitter can leverage the wavelength range around the peak so that a high TPV conversion efficiency can be obtained. However, an actual narrowband emitter does not possess such a stepwise emissivity spectrum. The emissivity for the targeted wavelength range may not reach 100%, and that for the remaining range is not totally zero as well.

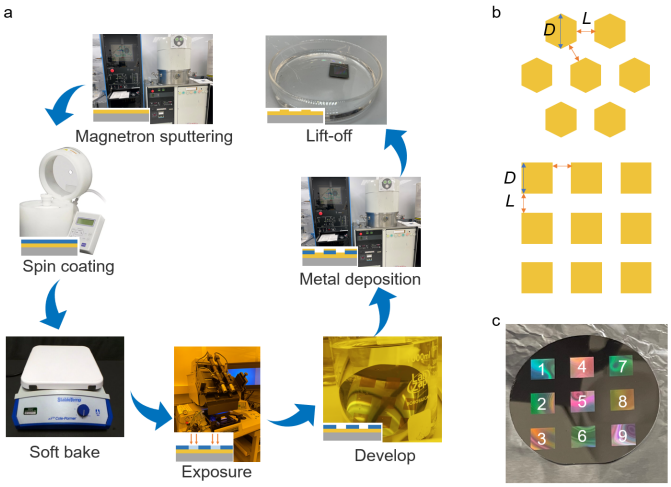

Fig. 2 (a) Fabrication process of the narrowband emitter. First, a tungsten substrate layer is deposited on the silicon wafer by magnetron sputtering. Photolithography is composed of four steps: spin-coating the photoresist, soft bake, exposure and development. Then another metal deposition is conducted, followed by the lift-off process. (b) Two types of patterned arrays for the photonic tungsten structure, with feature size D and gap L. (c) Optical image of 9 array patterns with different D and L built on a 3-inch silicon wafer. Each pattern has a square shape of 1.2 cm × 1.2 cm. Patterns 1–6 are hexagon arrays and patterns 7–9 are square arrays.

Since the TPV system needs to work at a high temperature, a refractory material like tungsten (W) is widely used for the TPV emitter. Here, we design a photonic tungsten structure on top of the tungsten substrate. Figure 2a shows the fabrication process, which is demonstrated in detail in the Experimental section. Two

types of patterned arrays (hexagon and square) are taken into consideration for the photonic tungsten structure, as shown in Fig. 2b. For either geometry type, there are two parameters: feature size D and gap L. Simulation work is conducted to study the effects of these two parameters. Besides, the patterned arrays are fabricated by the photolithography method. In Fig. 2c, 9 array patterns are built on a 3-inch silicon wafer, in which patterns 1–6 are hexagon arrays and patterns 7–9 are square arrays. The detailed geometric parameters for these 9 patterns are shown in Table 1.

Table 1 Geometric parameters for the 9 array patterns, including feature size D and gap L

Pattern	Structure	Feature size D (μm)	Gap L (μm)
1	Hexagon	1.2	0.8
2	Hexagon	1.2	1.0
3	Hexagon	1.2	1.2
4	Hexagon	1.3	0.8
5	Hexagon	1.4	0.8
6	Hexagon	1.6	0.8
7	Square	1.0	0.8
8	Square	1.0	1.0
9	Square	1.2	1.0

Next, a calculation study is conducted for the aforementioned 9 patterns. The calculation is performed by Finite-Difference Time-Domain (FDTD) method. The input source is a broadband plane wave. Periodic boundary conditions are employed along the boundaries that intersect the surface, and perfectly matched layer (PML) boundary conditions are applied in the out-of-plane direction. The plane wave is inserted as normal incidence. In thermodynamic equilibrium, wavelength-specific radiative emission equals absorption due to Kirchhoff's law. We perform the reflectance and transmittance spectra calculation by the FDTD lumerical software, and emissivity is obtained by subtracting these two wavelength-specific values from 1. Figure 3a demonstrates the emissivity spectra for the 6 hexagon patterns. In general, it is observed that emissivity is decreasing from around 0.5 to low emissivity in the wavelength range between 0.5 μm and 2.5 μm, which is consistent with bulk tungsten. However, there appear narrowband peaks located at a wavelength larger than 1.5 μm, which is due to the effect of surface plasmon polariton. Surface plasmons are oscillating charge densities on the metal surface. If a metal has a structured surface, such as the tungsten array patterns here, electromagnetic radiation can couple with surface plasmons. This leads to an increase in the emittance of a metallic surface in a limited spectral range. While towards longer wavelengths the grating has a low emissivity like a plane metal surface. Besides, this wavelength range matches the bandgaps of several TPV cells, such as GaSb (0.72 eV), InGaSb (0.60 eV) and InGaAsSb (0.54 eV), paving the way for TPV applications utilizing this spectral selectivity of high emissivity. As the feature size D is fixed, it is observed that the peaks shift to longer wavelength when the gap L increases (solid curves). As the gap L keeps constant as 0.8 μm, there also appears a red-shift for larger feature size D (dashed curves). Nevertheless, the bandwidths of these narrowbands show little difference from each other. Considering the square cases (Fig. 3b), it shows a similar peak-shift phenomenon. Either larger L or D leads to the peak red-shift, while having little impact on the bandwidth. The peak position of the surface plasmon resonance and the strength of this excitation depend on the grating period and the shape of the grating structures. The peak position is close to the diffraction wavelength, which at normal incidence is equal to the period[53], which means a larger period leads to a peak red-shift. Therefore, for the case of the square arrays, either a larger feature size D or a larger gap L with the other one kept fixed would cause the peak to shift to a longer wavelength. For the hexagon arrays, though the period is not exactly the sum of D and L, it still follows this trend. So far, all the calculations for Fig. 3a and b are based on constant pattern height h equal to 100 nm. Next, the influence of height is studied. In Fig. 3c and d, five height values are selected as 100 nm, 150 nm, 200 nm, 250 nm and 300 nm, respectively. Figure 3c is based on hexagon pattern P1 and Fig. 3d is based on square pattern P7. From these two figures, it is clearly shown that as the height is increased, the peak positions gradually move to a larger wavelength. The peak values reach the maximum with a height equal to 150 nm, and then keep decreasing when further increasing the height. Moreover, along with the emissivity reduction, the narrowband is becoming broader significantly.

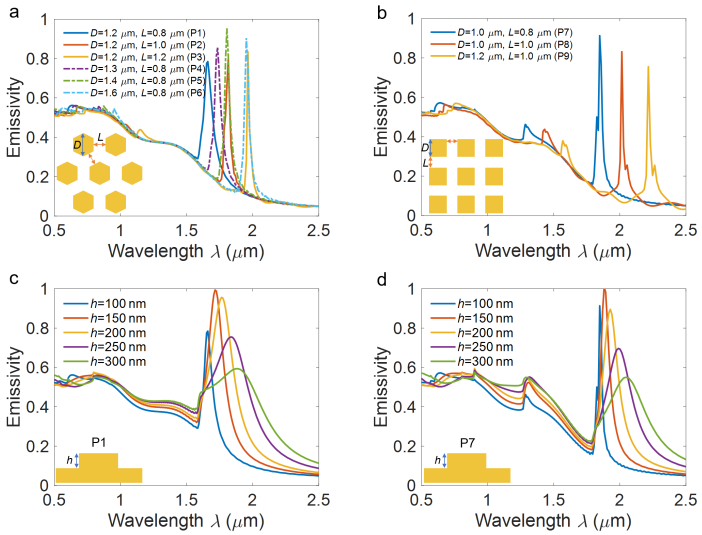

Fig. 3 Calculated emissivity spectra of the proposed narrowband emitter performed by FDTD method. Emissivity spectra for the (a) 6 hexagon patterns and (b) 3 square patterns when the pattern height h keeps constant at 100 nm. The influence of h on the emissivity spectra is based on (c) a hexagon pattern P1 and (d) a square pattern P7, respectively. Five height values are taken into consideration, including 100 nm, 150 nm, 200 nm, 250 nm and 300 nm.

From the calculation, we find that the position and bandwidth of the narrowband emission can be controlled by the geometric parameters of the tungsten photonic structure, including feature size D, gap L and height h. Thus, by properly selecting the parameters, the narrowband peak position can be specified to match the bandgap of some commonly used TPV cells, for example, GaSb (1.73 μm/0.72 eV), InGaSb (2.07 μm/0.60 eV), and InGaAsSb

(2.30 μm/0.54 eV). In Fig. 4, three emitters are chosen from the 9 patterns (P4, P6 and P9), which correspond to the three cells aforementioned respectively. Based on Wien's displacement law, we choose three blackbodies with different temperatures (1700 K, 1450 K and 1300 K) so that the blackbody peak wavelength can match with the narrowband. In this way, the narrowband emitter can radiate suitable photon energy as much as possible. The actual emitter spectral radiance is equal to the product of the blackbody radiation and the emissivity of the emitter, which is demonstrated as the shaded area corresponding to the solid and dashed curves with the same color. It is shown that significant photon energy emittance is within the narrowband, though there are quite a few photons with higher energy emitting out. As mentioned, the emissivity for an ideal TPV narrowband emitter is unity in the wavelength range corresponding to the TPV cell bandgap, while it is zero in the remaining range. However, the actual case is not perfect. The emitters discussed here significantly suppress the low-energy photons, while still possessing a moderate emissivity for high-energy photons, leading to a thermalization loss. The privilege is the blackbody radiation for these high-energy photons is relatively low, suppressing the actual emission and reducing thermalization loss to some extent.

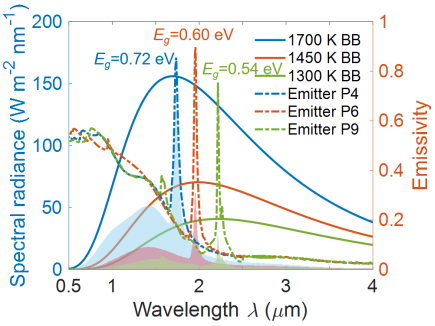

Fig. 4 Three emitters (P4, P6 and P9) with narrowbands are matched with the peak wavelengths of three blackbodies of different temperatures (1700 K, 1450 K and 1300 K). The emitters are also matched with the bandgap of some commonly used TPV cells: GaSb (1.73 μm/0.72 eV), InGaSb (2.07 μm/0.60 eV), and InGaAsSb (2.30 μm/0.54 eV). The shaded areas are the actual spectral radiance equal to the product of the blackbody radiation and the emissivity of the emitters with the same colors.

Next, array patterns with various geometric parameters listed in Table 1 are fabricated based on the process introduced in Fig. 2a. The patterns are built on a 3-inch silicon wafer. To evaluate the fabrication quality, the structure of the array patterns is characterized by scanning electron microscopy (Supra 25 SEM). Figure 5a and b show the square and hexagon patterns, respectively. Both samples are after development, while before metal deposition and lift-off. From the figures, it is observed that the resist is totally peeling off from the patterned areas, leaving the clear square and hexagon shapes. However, some fabrication defects may occur sometimes, like the round-corner issue, which is quite obvious in Fig. 5a. This is restricted by the photolithography wavelength and a feature size of around 1 μm is close to the highest resolution the mask aligner we used can work with.

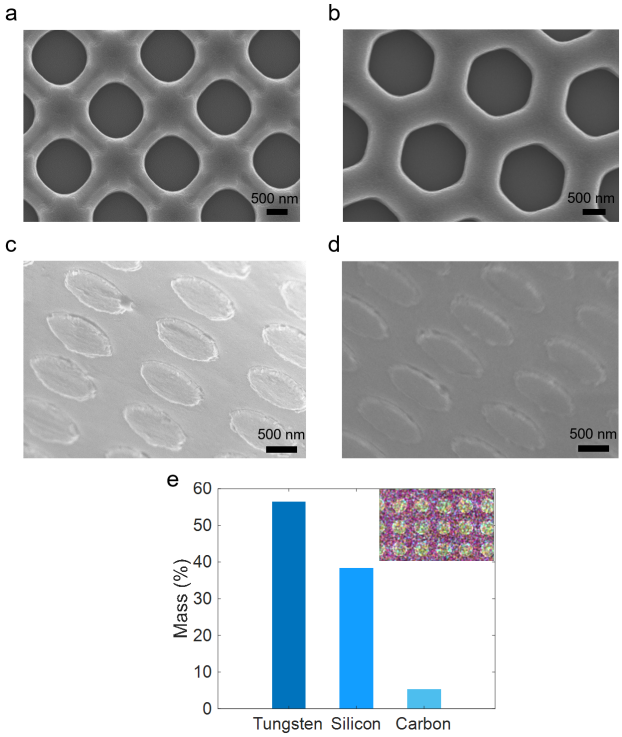

Fig. 5 SEM images of (a) square array and (b) hexagon array patterns after the photolithography process. Angle-tilted SEM images of (c) square array and (d) hexagon array patterns after the lift-off process. (e) Mass percentages of the fabricated emitter based on Energy Dispersive Spectroscopy (EDS) measurement. The inset is a SEM image with a colored overlay representing concentrations of different elements. Yellow stands for tungsten and pink stands for silicon.

Figure 5c and d show the angle-tilted SEM images of the square and hexagon patterns after the lift-off process. Energy Dispersive Spectroscopy (EDS) measurement is conducted to characterize the proportions of elements on the sample (Fig. 5e). This is the final sample after the lift-off process. Tungsten and silicon are primary components, which account for more than 94%. The inset shows that the tungsten is concentrated on the patterned structures, and the silicon is concentrated in between. The small amounts of carbon are probably due to resist residue.

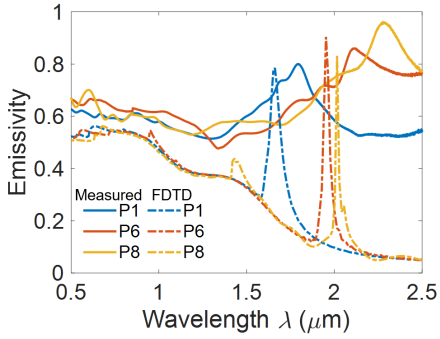

Fig. 6 Comparison between the measured emissivity (solid curves) and the calculated emissivity (dashed curves) based on three patterns (P1, P6 and P8).

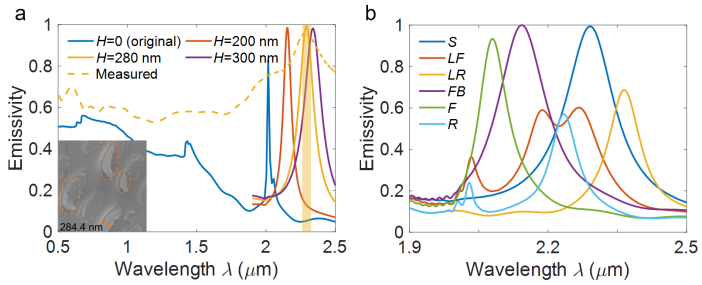

Fig. 7 (a) Calculated emissivity for the structure of assumed sidewalls circling around the original square pattern. The calculation is based on pattern 8 (square array, $D = L = 1$ μm). The sidewall width is selected as 50 nm and the height H is set as 200 nm, 280 nm and 300 nm, respectively. The inset SEM image shows the metal residue (sidewall). (b) Emissivity spectrum of different sidewall cases: surrounded (S), left-front (LF), left-right (LR), front-back (FB), front (F), and right (R). The wavelength is zoomed in to the range from 1.9 to 2.5 μm.

We measure the spectra of these fabricated samples utilizing the Jasco V770 spectrometer with the integrating sphere, and then compare them with the FDTD calculation results. In Fig. 6, three pattern emissivity spectra are shown: two for the hexagon array (P1, P6) and one for the square array (P8). The dashed curves are FDTD calculation results from Fig. 3, and the solid curves are the experimental measurement. In the wavelength range from 0.5 μm to 1.5 μm, the measured curves and the FDTD curves are generally consistent with each other. The curves decline slowly and the measured emissivity is a little higher than the calculated one. As the wavelength is greater than 1.5 μm, the calculated emissivity continues to reduce to 0.05 except the narrowband peaks. We observe the peaks for the measured curves, while there are several distinctions as compared with the calculated curves, which can be attributed to several reasons. First, all three peaks tend to shift to longer wavelengths though their relative positions are as predicted. One possible reason is the fabrication precision and limitation. In general, the fabrication quality is good, but as we check the angle-tilted SEM images to see if there is any metal residue after the lift-off process, we do observe sidewalls left (dashed circles in the inset of Fig. 7a), which is due to the bad conformity of tungsten sputtering.

To study the influence of the metal residue on the narrowband emitter, another FDTD simulation is conducted. Figure S1 shows a unit of the patterned array in the simulation. Here, pattern 8 is chosen for this simulation (square array, $D = L = 1$ μm), and the hexagon cases should have similar results. We design a "wall" circling around the square pattern to mimic the metal residue. The width of the "wall" is set as 50 nm and the height H is set as 200 nm, 280 nm and 300 nm, respectively. As shown in Fig. 7a, the effects of the metal residue will shift the narrowband to a longer wavelength compared with the original pattern ($H = 0$). Meanwhile, the bandwidth is substantially increased. This trend conforms to what we obtained in the measurement. Besides, a larger height contributes to a larger narrowband shift. As the height is 280 nm, the calculated peak position is almost the same as that of the measurement, and this height is consistent with the inset SEM images as well.

Next, some other metal residue (sidewall) cases are discussed based on pattern 8, since the residue is not all around the original pattern observed from the SEM image. The case we just discussed in Fig. 7a is referred to as the surrounded case (S), with four sidewalls circling around the original pattern. Other cases are with two sidewalls or just one sidewall left, including the left-front (LF), left-right (LR), front-back (FB), front (F), and right (R). The schematic of these sidewall cases can be found in Fig. S2. From Fig. 7b, it is shown that both the narrowband position and the bandwidth are strongly influenced by different sidewall cases. As a result, the narrowband is extended to a much wider band as shown in the measurement due to a combined effect of these metal residues. Therefore, we have verified that the large difference between simulation and measurement could be caused by the metal residue after the lift-off process. Besides, based on the SEM images, the feature size D could be sometimes larger than the design due to overexposing or redundant developing time, which could also influence the narrowband position. In one word, the fabrication precision matters a lot for this narrowband emitter.

3 Conclusions

In summary, this work studies the tungsten-based photonic structure narrowband emitter numerically and experimentally, which can be applied for thermophotovoltaic energy conversion. The emitter consists of two refractory layers, a tungsten thin film substrate and a tungsten patterned array. Two geometric types (hexagon and square) of the array patterns are designed and analyzed. A parametric study is conducted for different feature sizes D, gaps L and pattern heights h using the FDTD lumerical software. A peak-shift can be triggered by adjusting these geometric parameters, and the pattern height has a large influence on the bandwidth as well. Next, the narrowband emitter is fabricated by photolithography followed by metal deposition and lift-off. Clear hexagon and square array patterns are shown by the optical characterization. The emissivity spectra are measured by an UV-Visible/NIR spectrophotometer Jasco V770 and compared with the FDTD calculated results. This work sheds light on the research on the narrowband selective emitter and its potential application in thermophotovoltaic energy conversion.

There are some future work and a few limitations of this work to be improved. The thermal stability of this tungsten-based emitter needs to be verified, which is an important factor for the implementation of a TPV device. The metal-based sample could suffer from oxidation due to significant O_2 partial pressure under medium vacuum conditions[54], which would have a big influence on its emissivity. To maintain the thermal stability at a higher temperature (>1000°C), either a higher vacuum condition or refractory oxides as protection layers such as HfO_2 is required. To realize the more precise control of the array patterns, an optimized fabrication technique is needed. Etching-based pattern transfer or bilayer lift-off may help with better device fabrication.

4 Experimental section

4.1 Sample preparation

The fabrication process is demonstrated in Fig. 2a, and the sample at each step is shown as the inset for each procedure. The 3-inch wafers were from UniversityWafer, Inc. The wafers were first cleaned with acetone, isopropyl alcohol, and deionized (DI) water, then dried with nitrogen gas. A 100 nm tungsten layer was first deposited on the wafer by magnetron sputtering (MRC 8667). Then, positive photoresist Shipley 1813 was dropped on the wafer using a plastic pipette and spin-coated using Laurell Spinner. The spin speed was 5000 rpm and the spinning time was 60 s. The following step was soft bake at 115°C for 60 s. The exposure was performed using Quintel 4000 mask aligner, and the photolithography mask was from PhotomaskPORTAL. Then the wafer was soaked and developed in AZ 726 MIF developer for 60 s, followed by DI water rinsing and N_2 blowing. It was observed that the resist was peeling off from the exposed area since Shipley 1813 was a positive resist. Thus, patterned resist structures were achieved.

The next step was the metal deposition and lift-off process. We used magnetron sputtering to deposit 100 nm thick tungsten. The samples were cut into small pieces and soaked in acetone for lift-off. It would expedite the lift-off process with the help of ultrasonication.

4.2 Material characterization

In thermodynamic equilibrium, wavelength-specific radiative emission equals absorption due to Kirchhoff's law. Absorbance data were obtained by measuring the reflectance spectra of samples with the Jasco V770 spectrometer, using the Jasco ISN-923 integrating sphere at an angle of 6°. As samples are opaque, transmittance was assumed to be zero, and absorbance was obtained by subtracting the reflectance values from 1. The morphology and structure of the emitter sample were characterized by scanning electron microscopy (Supra 25 SEM). Chemical surface characterizations were performed using the Bruker Quantax EDS.

Author Contributions

Fangqi Chen: Conceptualization, Methodology, Software, Validation, Investigation, Writing – original draft. **Xiaojie Liu:** Conceptualization, Methodology, Validation. **Yang Liu:** Conceptualization, Methodology. **Yanpei Tian:** Conceptualization, Writing - review & editing. **Yi Zheng:** Conceptualization, Investigation, Supervision, Writing - review & editing.

Conflicts of interest

There are no conflicts to declare.

Acknowledgements

This project is supported by the National Science Foundation through grant number CBET-1941743 and the Defense Advanced Research Projects Agency through grant number W31P4Q-22-C-0014.

Notes and references

1 W. Shockley and H. J. Queisser, Journal of applied physics, 1961, **32**, 510–519.
2 H. Wang, J.-Y. Chang, Y. Yang and L. Wang, International Journal of Heat and Mass Transfer, 2016, **98**, 788–798.
3 N. M. Haegel, R. Margolis, T. Buonassisi, D. Feldman, A. Froitzheim, R. Garabedian, M. Green, S. Glunz, H.-M. Henning, B. Holder et al., Science, 2017, **356**, 141–143.
4 S. Wang, P. Wang, B. Chen, R. Li, N. Ren, Y. Li, B. Shi, Q. Huang, Y. Zhao, M. Grätzel et al., eScience, 2022.
5 M. Wang, H. Wang, W. Li, X. Hu, K. Sun and Z. Zang, Journal of Materials Chemistry A, 2019, **7**, 26421–26428.
6 Y. Miao, X. Wang, H. Zhang, T. Zhang, N. Wei, X. Liu, Y. Chen, J. Chen and Y. Zhao, eScience, 2021, **1**, 91–97.
7 B. Yang, M. Wang, X. Hu, T. Zhou and Z. Zang, Nano Energy, 2019, **57**, 718–727.
8 K.-L. Wang, Y.-G. Yang, Y.-H. Lou, M. Li, F. Igbari, J.-J. Cao, J. Chen, W.-F. Yang, C. Dong, L. Li et al., eScience, 2021, **1**, 53–59.
9 A. Ghanekar, L. Lin and Y. Zheng, Optics express, 2016, **24**, A868–A877.
10 M. M. A. Gamel, H. J. Lee, W. E. S. W. A. Rashid, P. J. Ker, L. K. Yau, M. A. Hannan, M. Jamaludin et al., Materials, 2021, **14**, 4944.
11 Z. Zhou, E. Sakr, Y. Sun and P. Bermel, Nanophotonics, 2016, **5**, 1–21.
12 Y. Xuan, X. Chen and Y. Han, Renewable Energy, 2011, **36**, 374–387.
13 Z. Utlu and U. Parali, Energy conversion and management, 2013, **74**, 308–322.
14 T. Bauer, I. Forbes and N. Pearsall, International journal of ambient energy, 2004, **25**, 19–25.
15 A. Datas, A. Ramos, A. Martí, C. del Cañizo and A. Luque, Energy, 2016, **107**, 542–549.
16 C. Amy, H. R. Seyf, M. A. Steiner, D. J. Friedman and A. Henry, Energy & Environmental Science, 2019, **12**, 334–343.
17 A. Datas and A. Martí, Solar Energy Materials and Solar Cells, 2017, **161**, 285–296.
18 X. Wang, R. Liang, P. Fisher, W. Chan and J. Xu, Journal of Propulsion and Power, 2020, **36**, 593–603.
19 A. De Pascale, C. Ferrari, F. Melino, M. Morini and M. Pinelli, Applied Energy, 2012, **97**, 695–703.
20 W. R. Chan, V. Stelmakh, C. M. Waits, M. Soljacic, J. D. Joannopoulos and I. Celanovic, Journal of Physics: Conference Series, 2015, p. 012069.
21 D. Chubb, Fundamentals of thermophotovoltaic energy conversion, Elsevier, 2007.
22 D. F. DeMeo, A. S. Licht, C. M. Shemelya, C. M. Downs and T. E. Vandervelde, Rectenna Solar Cells, Springer, 2013, pp. 371–390.
23 Z. Chen, P. L. Adair and M. Rose, IECEC-97 Proceedings of the Thirty-Second Intersociety Energy Conversion Engineering Conference (Cat. No. 97CH6203), 1997, pp. 1097–1100.
24 Y.-B. Chen and Z. Zhang, Optics communications, 2007, **269**, 411–417.

25 X. Liu, Z. Li, Z. Wang, H. S. Yun and S. Shen, Frontiers in Energy, 2022, 1–7.

26 X. Liu, L. Jing, X. Luo, B. Yu, S. Du, Z. Wang, H. Kim, Y. Zhong and S. Shen, Applied Physics Letters, 2022, **121**, 131703.

27 J. Li, B. Yu and S. Shen, Physical Review Letters, 2020, **124**, 137401.

28 Z. Wang, D. Kortge, Z. He, J. Song, J. Zhu, C. Lee, H. Wang and P. Bermel, Solar Energy Materials and Solar Cells, 2022, **238**, 111554.

29 B. Wang, M. Liu, T. Huang and C. Zhao, ES Energy & Environment, 2019, **6**, 18–38.

30 D. G. Baranov, Y. Xiao, I. A. Nechepurenko, A. Krasnok, A. Alù and M. A. Kats, Nature materials, 2019, **18**, 920–930.

31 R. Sakakibara, V. Stelmakh, W. R. Chan, M. Ghebrebrhan, J. D. Joannopoulos, M. Soljacic and I. Čelanović, Journal of Photonics for Energy, 2019, **9**, 032713.

32 O. M. Nielsen, L. R. Arana, C. D. Baertsch, K. F. Jensen and M. A. Schmidt, TRANSDUCERS'03. 12th International Conference on Solid-State Sensors, Actuators and Microsystems. Digest of Technical Papers (Cat. No. 03TH8664), 2003, pp. 714–717.

33 L. Fraas, J. Samaras, J. Avery and L. Minkin, Conference Record of the Twenty-Eighth IEEE Photovoltaic Specialists Conference-2000 (Cat. No. 00CH37036), 2000, pp. 1020–1023.

34 B. Bitnar, W. Durisch, J.-C. Mayor, H. Sigg and H. Tschudi, Solar Energy Materials and Solar Cells, 2002, **73**, 221–234.

35 D. M. Bierman, A. Lenert, W. R. Chan, B. Bhatia, I. Celanović, M. Soljačić and E. N. Wang, Nature Energy, 2016, **1**, 1–7.

36 A. Lenert, D. M. Bierman, Y. Nam, W. R. Chan, I. Celanović, M. Soljačić and E. N. Wang, Nature nanotechnology, 2014, **9**, 126–130.

37 W. R. Chan, V. Stelmakh, M. Ghebrebrhan, M. Soljačić, J. D. Joannopoulos and I. Čelanović, Energy & Environmental Science, 2017, **10**, 1367–1371.

38 V. Rinnerbauer, A. Lenert, D. M. Bierman, Y. X. Yeng, W. R. Chan, R. D. Geil, J. J. Senkevich, J. D. Joannopoulos, E. N. Wang, M. Soljačić et al., Advanced Energy Materials, 2014, **4**, 1400334.

39 A. Kohiyama, M. Shimizu and H. Yugami, Applied Physics Express, 2016, **9**, 112302.

40 M. Shimizu, A. Kohiyama and H. Yugami, Journal of Photonics for Energy, 2015, **5**, 053099.

41 Y. Tian, A. Ghanekar, M. Ricci, M. Hyde, O. Gregory and Y. Zheng, Materials, 2018, **11**, 862.

42 Y. X. Yeng, W. R. Chan, V. Rinnerbauer, J. D. Joannopoulos, M. Soljačić and I. Celanovic, Optics express, 2013, **21**, A1035–A1051.

43 V. Stelmakh, V. Rinnerbauer, R. Geil, P. Aimone, J. Senkevich, J. Joannopoulos, M. Soljačić and I. Celanovic, Applied Physics Letters, 2013, **103**, 123903.

44 L. Wang, S. Basu and Z. Zhang, Journal of heat transfer, 2012, **134**, 072701.

45 M. Langlais, H. Bru, P. Ben-Abdallah et al., Journal of Quantitative Spectroscopy and Radiative Transfer, 2014, **149**, 8–15.

46 H. Deng, T. Wang, J. Gao and X. Yang, Journal of Optics, 2014, **16**, 035102.

47 S. Wu, X. Li, Y. Zhan and K. Li, Optics Letters, 2014, **39**, 817–820.

48 L. Wang and Z. Zhang, Applied Physics Letters, 2012, **100**, 063902.

49 B. Zhao, L. Wang, Y. Shuai and Z. M. Zhang, International Journal of Heat and Mass Transfer, 2013, **67**, 637–645.

50 B. Jae Lee, Y.-B. Chen, S. Han, F.-C. Chiu and H. Jin Lee, Journal of heat transfer, 2014, **136**, 072702.

51 H. Wang, K. O'Dea and L. Wang, Optics letters, 2014, **39**, 1457–1460.

52 M. Yan, J. Dai and M. Qiu, Journal of Optics, 2014, **16**, 025002.

53 A. Heinzel, V. Boerner, A. Gombert, B. Bläsi, V. Wittwer and J. Luther, Journal of Modern Optics, 2000, **47**, 2399–2419.

54 M. Chirumamilla, G. V. Krishnamurthy, S. S. Rout, M. Ritter, M. Störmer, A. Y. Petrov and M. Eich, Scientific reports, 2020, **10**, 1–10.